AIP Journal of Applied Physics

Effect of mixed Ge/Si cross-linking on the physical properties of amorphous Ge-Si-Te networks

K. Gunasekera, P. Boolchand, and M. Micoulaut

Citation: Journal of Applied Physics **115**, 164905 (2014); doi: 10.1063/1.4871780
View online: http://dx.doi.org/10.1063/1.4871780
View Table of Contents: http://scitation.aip.org/content/aip/journal/jap/115/16?ver=pdfcov
Published by the AIP Publishing

Effect of mixed Ge/Si cross-linking on the physical properties of amorphous Ge-Si-Te networks

K. Gunasekera,[1] P. Boolchand,[1] and M. Micoulaut[2,a)]
[1]*School of Electronics and Computing Systems, College of Engineering and Applied Science, University of Cincinnati, Cincinnati, Ohio 45221-0030, USA*
[2]*Laboratoire de Physique Théorique de la Matière Condensée, Université Pierre et Marie Curie, 4 Place Jussieu, F-75252 Paris Cedex 05, France*

(Received 3 March 2014; accepted 8 April 2014; published online 25 April 2014)

Amorphous $Ge_xSi_xTe_{1-2x}$ glasses are studied as a function of composition by a combination of experimental and theoretical methods, allowing for a full description of the network structure in relationship with physico-chemical properties. Calorimetric and thermal measurements reveal that such glasses display an anomalous behavior across a range of compositions $x_{c1} = 7.5\%$ and $< x < x_{c2} = 9\%$, in which is manifested a deep minimum in molar volume, non-reversing enthalpy, and liquid fragility. These anomalies allow defining an intermediate phase, where network rigidity onsets as the content x of Group IV atoms (Ge, Si) are increased. The structural manifestation of these anomalies is understood from ^{119}Sn Mössbauer spectroscopy and First Principles Molecular Dynamics at selected compositions ($Ge_{20}Te_{80}$, $Si_{20}Te_{80}$, and $Ge_{10}Si_{10}Te_{80}$). The numerical models reveal the quite different roles played by the modifier or network cross-linker Ge or Si atoms, Si being more tetrahedral in sp^3 geometry, whereas Mössbauer spectroscopy shows that the nature of chemical bonding is dramatically changed around $x \simeq 8\%$. The precise evolution of the local structure and chemical bonding ultimately allows understanding the origin of the intermediate phase in these complex tellurides. © *2014 AIP Publishing LLC*. [http://dx.doi.org/10.1063/1.4871780]

I. INTRODUCTION

Compositional studies and the investigation of trends in physico-chemical properties with composition have proven to be a powerful experimental and theoretical approach in trying to understand network glasses at a fundamental level. This usually allows defining the glass formation region (GFR), where materials can be obtained by a standard melt quench to yield bulk glasses.[1,2] The GFR of chalcogenides is quite extensive,[3] so that a large number of combinations is possible using atoms from Groups III, IV, and V elements, which combine short atomic radii, light atomic masses, low ionicity, and a large number of electron lone-pairs, the latter property being used for the design of applications in optoelectronics[4–6] and memory devices.[7–9] It is also well known that the addition of heavy mass elements will reduce the GFR[10] but will increase the infrared transmission[11] and will reduce the optical energy gap of the chalcogen, which is ideal for semiconducting and optical applications.[12,13] The nature of the network structure of light amorphous chalcogenides, sulfur- or selenium-based, has been quite successfully described using rigidity theory,[14–16] which reduces the complex N-body problem to a connectivity one involving the underlying network topology. This allows filtering out unnecessary details, which ultimately do not affect the compositional trends, while focusing only on the key microscopic physics governing the thermal and mechanical properties. This approach has enabled accurate predictions of glass compositions, where elastic phase transitions can be expected,[17,18] and many other physical properties that have a bearing on these elastic phase transitions have also been investigated in a large number of binary or ternary sulphides[19–23] and selenides,[24–28] as well as oxides[29–33] and even commercial glasses.[34–37]

According to rigidity theory,[14–16] the GFR and glass-forming ability are determined by comparing the number of atomic degrees of freedom n_L per atom with the number of interatomic force field constraints n_c arising from bond-stretching (BS) and bond-bending (BB) interactions, which constrain[17,18,38,39] the network structure at a molecular level. If the number of constraints n_c is less than the available degrees of freedom (3 in 3D), then the network is viewed to be "*flexible*," because it contains local deformation modes that give rise to well-identified low frequency modes in the vibrational density of states.[40,41] On the opposite, if $n_c > 3$, the network becomes overconstrained or "*stressed rigid*," this situation being achieved when a high density of cross-linking atoms has been alloyed into a base chalcogen network. Interestingly, *optimal glasses* are identified with compositions fulfilling exactly $n_c = 3$, a condition that coincides with the isostatic stability criterion enunciated in the late 19th century by Lord Maxwell for macroscopic structures.[42] The term of "*optimal glasses*"[38,43] may be viewed as a vague notion at a first glance, but it actually encompasses various kinds of observed phenomena. These indicate that the glass-forming tendency or glass stability[1,2] is, indeed, enhanced for such particular isostatic compositions, and are revealed by a minimum with composition in the critical cooling rate[44–46] to avoid crystallization, or by a maximum[47,48] in the thermal stability $\Delta T = T_x - T_g$, where

a)Author to whom correspondence should be addressed. Electronic mail: mmi@lptl.jussieu.fr

T_x is the crystallization temperature and T_g is the glass transition temperature.

Building on these elegant ideas, there has been a vast body of experimental studies, in this context, on sulfide[19–23] and selenide[24–28] network glasses, and most of them have shown that anomalies are found in compositional studies at the location of the isostatic criterion, i.e., when $n_c = 3$, a result that has been associated by Phillips[38] and Thorpe[17,18] with a mean-field flexible to stressed rigid transition occurring at a network mean coordination number $\bar{r} = 2.4$, e.g., at $x = 20\%$ Ge content[49,50] in Ge_xSe_{1-x}.

Much less is known on amorphous tellurides, which, furthermore, display reduced GFRs[3] or, in some selected cases, no GFR at all, leading to systematic crystallization of the melts[51,52] directly upon cooling. This may be related to the increased tendency of elemental tellurium melt[53] to crystallize, as compared to sulfur and selenium, and by the fact that the heavier chalcogen does not strictly follow the so-called octet or "8-$\mathcal{N}$" bonding rule, $\mathcal{N}$ being the number of s and p electrons. These conditions also prevent estimating n_c and $\bar{r}$ in a simple fashion, and, thus, using directly rigidity theory to investigate effects of composition in tellurides, given that the ionocovalent to metallic nature of the bonding reduces its applicability. Attempts to quantify the number of rigid constraints have been made on a heuristic basis[54] but results seem to lead to an obvious disagreement with experiments.[9,55] More recently, a Molecular Dynamics (MD) based approach has been proposed to address the issue.[56] It builds on the notion of radial and angular excursions[57,58] to estimate correctly the number of intact BS and BB constraints, and an application to Ge-Sb-Te ternary alloys[56] has shown that, indeed, the Te-rich compositions should be flexible, whereas a flexible to rigid transition should be obtained close to the $GeTe_4$-$SbTe_4$ join. However, testing the generality of the concepts and methods to amorphous binary and ternary tellurides[59] has been challenging.

In the present contribution, we investigate the properties of $Ge_xSi_xTe_{1-2x}$ glasses as a function of composition x. The Ge-Si-Te ternary has not received much attention in the literature, except in the recent years. Feltz and co-workers[60,61] have characterized its glass-forming region, which consists in a broad region around the $GeTe_4$-$SiTe_4$ join. More recently, Asokan and co-workers have identified that such tellurides can also be interesting candidates for random access memories[62–64] because they exhibit on- and off-reset states in electrical switching phenomena that are enhanced at select compositions. A connection of such electrical properties with the elastic nature of the network, from flexible to stressed rigid has been established,[65] including an intermediate phase[66] where mechanical properties displayed a plateau-like behavior.[67]

In this paper, experimental measurements, usually undertaken in selenide and sulfides to detect rigidity transitions, are successfully combined with the constraint count established in a neat way from MD simulations to extend results to Tellurides for the first time. The constraint count in Tellurides differs from the one routinely applied in sulfide and selenide glasses using the 8-$\mathcal{N}$ bonding rule. Results show that, while Ge and Si are indeed four-fold coordinated, their local geometry are quite different and consist principally of defect octahedral (pyramidal) and tetrahedral units, respectively. The population of these geometries is computed using angular excursions and constraints. Such findings are directly compared to results from Mössbauer spectroscopy, which provides a quantitative estimate of the sp^3 coordinated cations as a function of composition. The structural picture that emerges from these findings obviously modifies the topological constraint count based on the 8-$\mathcal{N}$ bonding rule alone,[68] and shows an adaptive behavior with a progressive Ge/Si tetrahedral to pyramidal geometry conversion when the network stiffens. Experimentally, the flexible to rigid transition is then detected from calorimetric and volumetric measurements, which show anomalies (i.e., minima) in the non-reversing enthalpy ΔH_{nr} at the glass transition, molar volume V_m, and fragility $\mathcal{M}$ over a finite compositional interval Δx centered near $x = 8\%$. Furthermore, the square-well like behavior with composition of both ΔH_{nr} and V_m allows for the unambiguous detection of a previously reported intermediate phase (IP), which is systematically detected between the flexible and the stressed rigid phase.[69,70] The observed IP is quite sharp ($\Delta x \leq 2\%$) as compared to corresponding selenides and sulfides.[16] Finally, we detect important variations in the geometrical motifs (tetrahedra, defect octahedra) across the IP, thus indicating that the onset of stressed rigidity affects not only the local structure in tellurides, but also the nature of chemical bonding.

Taken together, the results reveal the richness of structural motifs encountered in these ternary tellurides, but, ultimately, also show that the well-established phenomenology largely described in lighter chalcogenides (S, Se) extends to the complex tellurides as also emphasized recently.[47,48,71] These new findings, thus, open the perspective that tellurides from the viewpoint of topology and rigidity can be examined in much the same fashion as selenides and sulfides. A major drawback however is the increased crystallization tendency of tellurium,[53] which prevents experimental investigations into the flexible phase down to $x = 0$, or elemental Te in bulk glasses. On the theoretical side, one needs to rely on a combination of realistic MD-based structural models and a constraint count from radial- and angular excursions in order to determine in a neat way the mean-field Maxwell rigidity transition.

The article is organized as follows: in Sec. II, we describe the experimental methods and techniques, and detail the First Principles MD (FPMD) simulation schemes. We provide all the results on structure and topology in Sec. III, and connect them to experimental observations in Secs. III E and IV. In Sec. V, we discuss our findings, and analyze the connection between topology, constraint count, and the obtained compositional thresholds. Finally, in Sec. VI, we summarize our results and draw a general perspective on extending topological rigidity theory to the Tellurides.

II. METHODS

A. Synthesis of glasses

Elemental of Si, Ge, and Te of 99.999% purity were reacted at 950 °C for periods ranging from 7 to 14 days. Due

to the low glass forming tendency of this system, batch sizes were kept at 0.5 g, which proved to be quite useful to obtain homogeneous glasses. Fig. 1 summarizes T_g data of $Si_xGe_xTe_{100-2x}$ system after 7 days (blue symbols) and 14 days (red symbols) of reacting starting materials. T_g's monotonically increase in $6\% < x < 12\%$ range and decrease once $x > 12\%$. Slight increases in T_gs were observed when samples were reacted for 14 days. The variation of T_g with composition in the Te-rich domain can be extrapolated down to $T_g(x = 0) = T_0 = 373$ K, a value, which is found to be of the order of other extrapolations (340 K (Ref. 72)). Stochastic agglomeration theory[73,74] leads to the prediction of the T_g variation with composition (solid black line in Fig. 1) assuming a random crosslinking of Ge/Si atoms is fulfilled up to nearly $x = 8\%$. At larger modifier content, random connections stop as manifested by the deviation of the T_g data with respect to the linear slope prediction.

B. Mössbauer spectroscopy

To the best of our knowledge, previous investigations in tellurides using this technique have been reported only for selected compositions of Si-Te glasses[76] using ^{125}Te and ^{129}I substitution. Here, one uses ^{119}Sn Mössbauer spectroscopy. A ^{119}Sn source of 23.8 keV γ rays in a $CaSnO_3$ matrix was used to excite the nuclear resonance using a constant acceleration drive. The emitter and glass sample absorber were cooled to 78 K in a He exchange gas Dewar. For the measurements, the bulk glasses were doped with 1 at. % of isotopically enriched ^{119}Sn metal. Observed spectra were analyzed to extract the isomer shift δ and quadrupole splitting Δ (see below). These data were compared to reference compounds having either a perfect tetrahedral geometry (c-Si, sp^3) or an octahedral geometry (c-SnTe, Sn^{2+}) for the Sn probe atoms.

C. Modulated differential scanning calorimetry

Melt fragility $\mathcal{M}$ of the $Si_xGe_xTe_{1-2x}$ system was established by recording the complex C_p heat flow (real, imaginary parts) near T_g using a TA Instruments Q2000 MDSC system. A 10 mg quantity of a glass sample sealed in an aluminum pan was cooled starting from $T_g + 50\,^\circ$C across the glass transition temperature and then heated back to $T_g + 50\,^\circ$C. Such experiments were undertaken at 5 modulation periods (60 s, 80 s, 100 s, 120 s, and 140 s). It should be stressed that the choice of the modulation periods limits the investigation of the relaxation time τ to temperatures that are very close to T_g so that only the linear behavior of the relaxation time in an Arrhenius plot is obtained. However, using the definition of the fragility[75] in this linear régime

$$\mathcal{M} \equiv \left[\frac{d\log_{10}\tau}{dT_g/T}\right]_{T=T_g}, \tag{1}$$

where the behavior of the relaxation time with temperature, $\tau(T)$, could be used to measure $\mathcal{M}$ as a function of composition x.

Total, reversing and non-reversing heat flow measurements were carried out using the same calorimeter. MDSC unit was calibrated for temperature and enthalpy using In and Pb standards, and for heat capacity using a Saphire disk. Heat flow measurements were carried out at a scan rate of 3 °C/min, modulation of amplitude of 1 °C and a period of 100 s. To correct a finite modulation frequency, a subsequent cooling cycle was carried out soon after the heating cycle.[77,78] The subtraction of the reversing heat flow from the total heat flow led to the nonreversing heat flow ΔH_{nr} following a procedure established previously.[79,80]

D. Molar volumes

Mass density measurements were made using 200 mg of a bulk glass to achieve an accuracy of 0.25%, which led to the molar volume after inversion. These were performed on the bulk $Si_xGe_xTe_{1-2x}$ glasses using a quartz fiber and a digital microbalance model B154 from Mettler-Toledo. A bulk glass specimen typically 200 mg in size was weighed in air and in 200 proof alcohols, and the density obtained using Archimedes principle. A single crystal of Si was used to calibrate the density of alcohol and a single crystal of Ge used to check the accuracy of density measurements.

E. First principles molecular dynamics

FPMD simulations have been performed at constant volume on three systems containing 200 atoms: $Si_{10}Ge_{10}Te_{80}$, $Ge_{20}Te_{80}$, and $Si_{20}Te_{80}$, the latter binary systems being used for comparison and reference. The atoms have been positioned in a periodically repeated cubic cell, whose size allows recovering the experimental measured volumes of $Si_{10}Ge_{10}Te_{80}$ (present work, see Table I and Fig. 12 below), and those reported for the binaries.[81,82] The electronic structure has been described within density functional theory (DFT) and evolved self-consistently during the motion.[83] A generalized gradient approximation is used, using an improved scheme for the exchange-correlation energy obtained by Perdew, Burke, and Ernzerhof (PBEsol) that has previously been used for the study of elemental tellurium,[84]

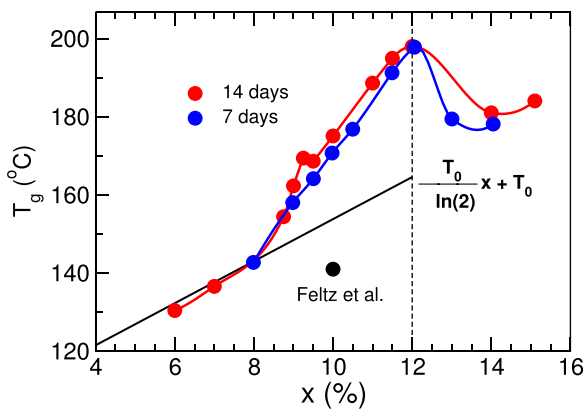

FIG. 1. Glass transition temperature T_g of $Ge_xSi_xTe_{1-2x}$ as a function of composition x, measured after 7 days (blue) and 14 days (red) of alloying the starting material. Other data ($Si_{10}Ge_{10}Te_{80}$) are from Feltz *et al.*[60] The vertical broken line shows the T_g maximum with nanoscale phase separation occurring at $x > 12\%$. The solid line represents the predicted slope equation using stochastic agglomeration theory. Here, T_0 represents $T_g(x = 0)$.

TABLE I. Calculated structural properties of different binary and ternary telluride glasses: $Ge_{20}Te_{80}$, $Si_{10}Ge_{10}Te_{80}$, and $Si_{20}Te_{80}$. Density ρ used in the simulation, calculated d_i first ($i=1$) and second ($i=2$) neighbour peak positions (in Å) of the partial pair correlation function $g_{ij}(r)$, together with obtained first minimum r_m of each $g_{ij}(r)$, and corresponding calculated coordination numbers n_{ij}. Note that the distances in $Si_{20}Te_{80}$ are compared to the experimental data of $Si_{19}Te_{81}$.[91]

	ρ(Å^{-3})		d_1^{th}	d_2^{th}	r_m	n_{ij}
$Ge_{20}Te_{80}$	0.0305 (Ref. 81)	Ge-Ge	2.48	3.72	3.01	0.33
			2.50 (Ref. 90)			
		Ge-Te	2.64	3.93	3.30	3.84
			2.60 (Ref. 90)			
		Te-Te	2.90	4.04	3.35	1.94
			2.76 (Ref. 90)			
$Si_{10}Ge_{10}Te_{80}$	0.0286	Ge-Ge	2.53	3.53	2.85	0.20
	Present	Ge-Te	2.64	3.99	3.21	3.36
	Work	Te-Te	2.85	4.10	3.26	1.58
		Si-Si	2.42	3.32	2.83	0.40
		Si-Te	2.61	3.99	3.13	3.12
		Si-Ge	2.45	4.02	3.08	0.35
$Si_{20}Te_{80}$	0.0267 (Ref. 82)	Si-Si	2.42	3.45	2.83	0.65
			2.44 (Ref. 93)			
		Si-Te	2.58	4.11	3.12	3.32
			2.62 (Ref. 91)			
		Te-Te	2.87	4.08	3.34	1.64
			2.82 (Ref. 93)	3.65 (Ref. 91)		

and has shown an improved agreement of structural properties when compared to experimental measurements from neutron diffraction. Valence electrons have been treated explicitly, and the wave functions have been expanded at the Γ point of the supercell on a plane wave basis set with an energy cutoff $E_c = 20$ Ry. During the Car-Parrinello Molecular Dynamics simulation, a fictitious electron mass of 2000 a.u. and a time step of $\Delta t = 0.24$ fs have been used to integrate the equations of motion. Temperature control has been implemented for both the ionic and electronic degrees of freedom by using Nosé-Hoover thermostats[85] with a frequency of 800 cm^{-1}.

In addition, an attractive empirical dispersion coefficient correction[86] has been taken into account, following the functional form proposed by Grimme

$$E_{disp} = -s_6 \sum_{i=1}^{N-1} \sum_{j=i+1}^{N} \frac{C_{ij}}{R_{ij}^6} f_{dmp}(R_{ij}), \tag{2}$$

where N is the number of atoms of the system, C_{ij} is the dispersion coefficient for atom pair ij, and R_{ij} is the interatomic distance. A damping function of the form

$$f_{dmp}(R_{ij}) = \frac{1}{(1+\exp(-d(R_{ij}/R_c - 1))} \tag{3}$$

is also used in order to avoid singularities at short interatomic distances. Here, R_c is a cutoff distance cancelling E_{disp} for $R < R_c$. Parameters for the (Ge, Te) systems (R_c, C_{ij}, d_{ij}) are given in Ref. 87, and for the ternary and the binary Si-Te, one, furthermore, has $C_{ij} = 95.43$, 176.97, and 129.90 eV · Å^{-6}, and $R_{ij} = 3.43$, 3.44, and 3.61 Å for Si-Si, Si-Te, and Si-Ge pairs, respectively.[86] Additional runs have been performed on Ge-Te without Eq. (2) for comparison (see below).

Starting configurations represent a random structure of (Ge, Si) and Te atoms fulfilling the desired stoichiometry, and the loss of the memory of the initial configurations has been achieved through preliminary runs at 2000 K and 1500 K over 50 ps. The chosen time interval leads to corresponding mean square displacements of the order of several cell lengths. After equilibrating the liquid at several temperatures (920 K, 820 K) over 25–30 ps each, all the systems have been brought to 300 K by two independent quenches from 820 K.

III. A STRUCTURAL MODEL

A. Global structure from FPMD

In Fig. 2, we represent the total pair correlation function g(r) and the total structure factor S_T(k) for the three simulated glasses of interest. These calculated quantities are compared to available experimental data from neutron and X-ray diffraction.[88,89]

First, we remark that the overall agreement between simulation and experiment is very good, and certainly improved when dispersion forces (via an explicit account of Eq. (2)) are treated during the DFT calculation. In fact, in $Ge_{20}Te_{80}$, a direct comparison with the experimental data from Kaban *et al.*[88] shows that while the first peak located at 2.69 Å in the experimental pair correlation function g(r) is quite well reproduced without the Grimme correction (green curve), the broadening of the first peak and a less structuration (minimum at ≃3.3–3.4 Å) will automatically lead to coordination numbers that are overestimated with respect to an experimental estimate[88] or a Reverse Monte Carlo analysis.[90] Definitely, the correction (2) improves the structural description of the short range order.

In real space (Fig. 2(a)), it is found that the structure of the ternary $Si_{10}Ge_{10}Te_{80}$ (solid and broken curves) is very close to the one of the binary $Si_{20}Te_{80}$ as seen from a nearly identical position and width of the principal peaks, found at 2.61 Å and 4.10 Å, and a nearly superimposition of both pair correlation functions at higher distances. A recent investigation of the liquid structure (923 K) has shown[93] that two typical peaks are found at 2.44 Å and 2.82 Å associated with Si-Te and Te-Te correlations, while the secondary peak is found at the same distance of 4.10 Å as in our amorphous phase. The position of the simulated first peak is also consistent with the one determined (2.62 Å) from X-ray diffraction for glassy $Si_{19}Te_{81}$,[91,92] whereas the secondary peak appears to be slightly overestimated (3.65–3.70 Å (Ref. 91)). The weak difference between the pair correlation function of $Si_{20}Te_{80}$ and $Si_{10}Ge_{10}Te_{80}$ contrasts with the comparison between the binary $Ge_{20}Te_{80}$ and the ternary, where

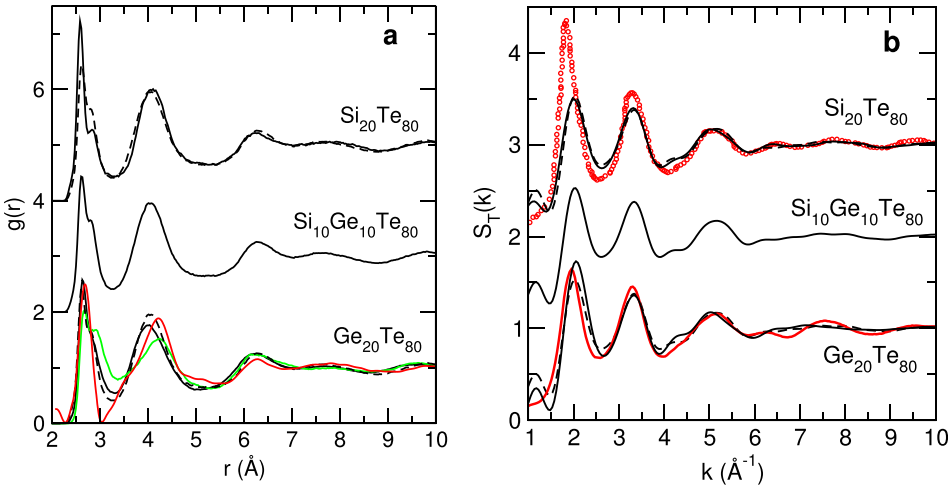

FIG. 2. (a) Computed total pair correlation function g(r) of $Ge_{20}Te_{80}$, $Si_{10}Ge_{10}Te_{80}$, and $Si_{20}Te_{80}$ (black lines) at 300 K, compared to neutron diffraction data from Kaban *et al.*[88] (red curve). (b) Computed total structure factor $S_T(k)$ for the three systems, compared to X-ray diffraction data from Schoening[89] ($Si_{20}Te_{80}$, red circles) and Kaban *et al.*[88] ($Ge_{20}Te_{80}$, red curve). The data of the ternary $Si_{10}Ge_{10}Te_{80}$ system have been duplicated (broken lines) in order to be directly comparable to the related binary systems. The green line in panel (a) is a simulation, which does not take into account the dispersion term of Eq. (2).

increased differences appear, and which underscore larger structural differences, including on the local structure.

A similar situation holds in reciprocal space, where $Si_{10}Ge_{10}Te_{80}$ and $Si_{20}Te_{80}$ have basically an identical total structure factor $S_T(k)$. However, when partial correlations are considered between the species (Faber-Ziman partial structure factors $S_{ij}(k)$), it can be seen that differences appear between these two systems (Fig. 3). Given the concentrations of the species and the involved neutron scattering lengths b_i (4.149, 8.185, and 5.68 fm for Si, Ge, and Te, respectively), it is first useful to write the total structure factor

$$S_T(k) = 0.0051(6)S_{SiSi} + 0.1129(7)S_{SiTe} + 0.6186(1)S_{TeTe} + 0.0200(7)S_{GeGe} + 0.2228(6)S_{GeTe} + 0.02055(1)S_{GeSi}. \quad (4)$$

Thus, $S_T(k)$ mostly results from Si-Te, Ge-Te, and Te-Te partials. In fact, the other pairs (Ge-Ge, Si-Si, Ge-Si) contribute only about $\simeq 5\%$ to $S_T(k)$. A comparison between $Si_{10}Ge_{10}Te_{80}$ (black lines) and $Si_{20}Te_{80}$ (red lines) in Fig. 3 shows that important differences appear in the region of

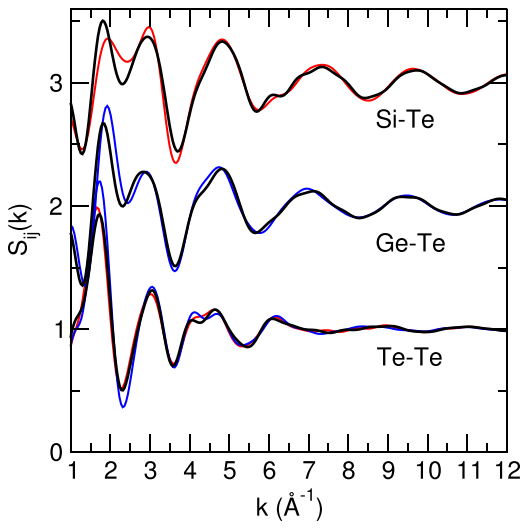

FIG. 3. Calculated partial structure factors $S_{SiTe}(k)$, $S_{GeTe}(k)$, and $S_{TeTe}(k)$ in $Ge_{10}Si_{10}Te_{80}$ (black), $Si_{20}Te_{80}$ (red), and $Ge_{20}Te_{80}$ (blue).

$\simeq 2.5$ Å^{-1} for the partial Si-Te, the binary system exhibiting a smaller separation between the two principal peaks of $S_{SiTe}(k)$ found at 1.7 Å^{-1} and 2.9 Å^{-1}. Furthermore, the peak heights are different, the first peak at $\simeq 2$ Å^{-1} being higher in the ternary, whereas the second peak (3 Å^{-1}) is smaller. However, given the dominant contribution of the Te-Te structure factor, which is nearly identical for both systems, ultimately such differences do not appear in the simulated $S_T(k)$. One can, thus, conclude that intermediate range correlations between Si and Te atoms are indeed different in the two systems under consideration. The comparison between $Si_{10}Ge_{10}Te_{80}$ (black lines) and $Ge_{20}Te_{80}$ (blue lines) shows that increased differences emerge in both relevant partials, Ge-Te and Te-Te, and these differences give rise to those obtained in the total structure factor (Fig. 2(b)).

In real space, a similar one to one comparison is made for the partial pair correlation functions $g_{ij}(r)$ (Figs. 4 and 5), and corresponding bond lengths are compared and analyzed (Table I). Obviously, the structural correlations (i.e., $g_{ij}(r)$) involving at least a Te atom (Fig. 4) are very similar for all the considered systems, e.g., weak differences are observed when the Te-Te correlation is compared between the ternary and corresponding binaries. Similarly, the Ge-Te pair correlation function of $Si_{10}Ge_{10}Te_{80}$ is almost identical to the one calculated for $Ge_{20}Te_{80}$. As a result, the calculated bond distances d_1 and d_2, which correspond to the first two peaks of each considered function $g_{ij}(r)$, are very close (Table I). The partial Si-Si deserves some additional comments given that the obtained features are very close to those usually observed in $GeSe_2$. In the latter system, three distances are usually detected[93,95] in the partial pair correlation function $g_{GeGe}(r)$, which are associated with homopolar Ge-Ge, edge-sharing (ES) $GeSe_{4/2}$ tetrahedra and corner-sharing (CS) tetrahedra (Fig. 6). In the present case, three typical distances are also obtained in the function $g_{SiSi}(r)$ of Fig. 5. In $Si_{10}Ge_{10}Te_{80}$, the first one at $d_1 = 2.42$ Å corresponds to the homopolar Si-Si bond that is also obtained ($\simeq 2.3$ Å) in the crystalline phase Si_2Te_3.[96] The second distance at $d_2 = 3.32$ Å in g_{SiSi} is the one associated with ES of predominantly tetrahedral $SiTe_{4/2}$ motifs, and, finally, the distance $d_3 = 3.89$ Å corresponds to CS connections between Si polyhedra. It is useful to anticipate that

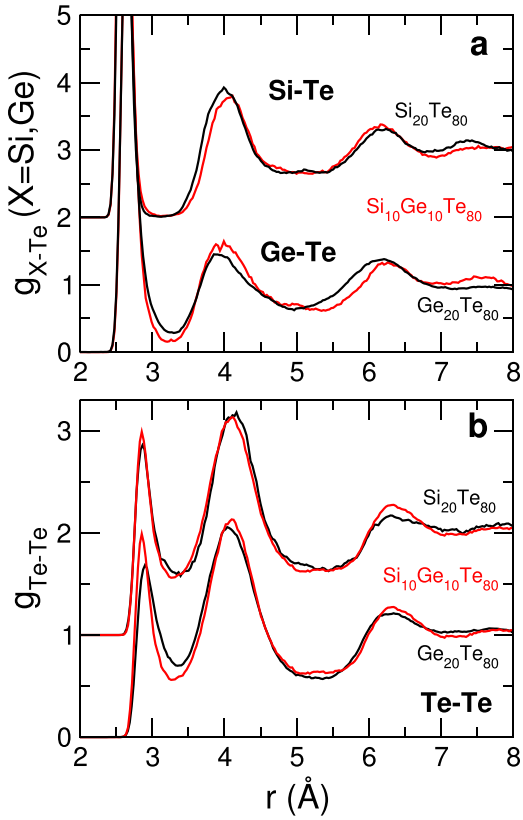

FIG. 4. Te-related partial pair correlation function g_{SiTe}, g_{GeTe} (a) and g_{TeTe} (b) of amorphous $Si_{10}Ge_{10}Te_{80}$ (red), and $Si_{20}Te_{80}$ and $Si_{20}Te_{80}$ (black).

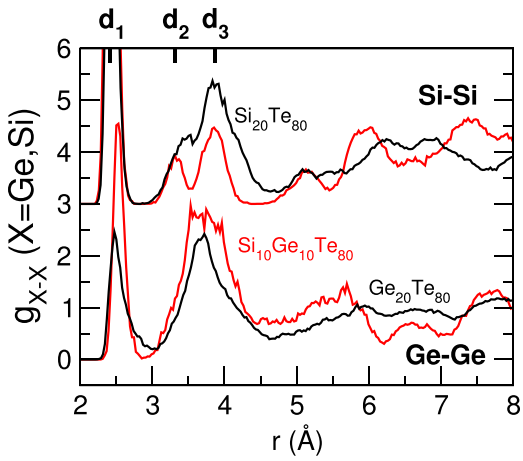

FIG. 5. Calculated Group IV-related partial pair correlation function g_{SiSi}, and g_{GeGe} of amorphous $Si_{10}Ge_{10}Te_{80}$ (red), and $Si_{20}Te_{80}$ and $Ge_{20}Te_{80}$ (black). The three typical distances d_1, d_2, and d_3 are indicated (see text for details).

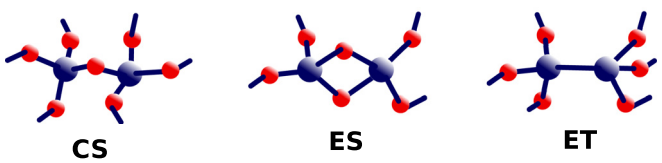

FIG. 6. Typical local connections between two Si units: CS $SiTe_{4/2}$, ES, and ethylene-like (ET) unit involving a homopolar Si-Si bond.

the well-separated peaks in $g_{SiSi}(r)$ should lead to typical bond angles associated with ES and CS connections, similar to the case of lighter chalcogenides.[93]

In the corresponding $Si_{20}Te_{80}$ binary compound, the two larger distances d_2 and d_3 come closer together so that the two associated typical ES and CS peaks merge into a single broad one, where the ES contribution appears only as a shoulder (black curve, Fig. 5). This effect cannot be attributed to the difference in density between the binary ($\rho = 0.0267\,\text{Å}^{-3}$) and the ternary ($\rho = 0.0286\,\text{Å}^{-3}$) compounds, and must therefore be associated with deeper changes in the network structure.

B. Neighbors

From the obtained simulated pair correlation functions (Figs. 4 and 5), we obtain by integrating up to corresponding first minima r_m (see Table I), the partial coordination numbers n_{ij} for the different systems using

$$n_{ij} = 4\pi\rho\int_0^{r_m} r^2 g_{ij}(r)dr. \tag{5}$$

It is seen that the dominant contribution to Ge and Si coordination number arises from the connections with Te atoms (i.e., n_{XTe} with X = Ge/Si). From such calculated coordination numbers n_{ij}, we then determine the coordination number of the species, which are given by

$$\begin{aligned} n_i &= n_{ii} + n_{ij}, \\ c_i n_{ij} &= c_j n_{ji}. \end{aligned} \tag{6}$$

In the ternary $Si_{10}Ge_{10}Te_{80}$ glass, it is found that $n_{Ge} = 3.91$, $n_{Si} = 3.87$, and $n_{Te} = 2.39$ indicating that, while Ge and Si atoms are predominantly in a four-fold coordination, Te has a slightly higher coordination number than what would be expected from the simple application of the 8-$\mathcal{N}$ bonding rule. Furthermore, although it is found $n_i \simeq 4$ for both Ge and Si, one is not a fully tetrahedral sp^3 geometry as characterized and discussed below. These numbers are found to be somewhat lower than those calculated from the corresponding binary glasses since we have obtained $n_{Si} = 3.97$ and $n_{Te} = 2.47$ for amorphous $Si_{20}Te_{80}$, and $n_{Ge} = 4.17$ and $n_{Te} = 2.90$ for $Ge_{20}Te_{80}$. As seen from Table I, the difference in Te coordination arises from increased contributions to n_{TeTe}, and for, e.g., $n_{TeGe} = n_{GeTe}/4$, which results from larger minima r_m and from a less structured pair correlation function, i.e., $g_{GeTe}(r_m)$ is larger in $Ge_{20}Te_{80}$ as compared to $Si_{10}Ge_{10}Te_{80}$.

C. Bond angle distribution

In Fig. 7, we represent the bond-angle distribution for the three systems of interest. The binary systems $Si_{20}Te_{80}$ and $Ge_{20}Te_{80}$ are found to display already quite a different behavior for both Te-X-Te and X-Te-X (X = Ge, Si). In fact, for the $Si_{20}Te_{80}$ system, one finds the silicon atom to be predominantly in a tetrahedral environment as revealed by a rather sharp Te-Si-Te distribution, which peaks at an angle of $\simeq 111°$, i.e., close to the tetrahedral angle of 109°21′. This feature is apparently maintained in the ternary $Si_{10}Ge_{10}Te_{80}$ given that both distributions nearly map onto each other. The

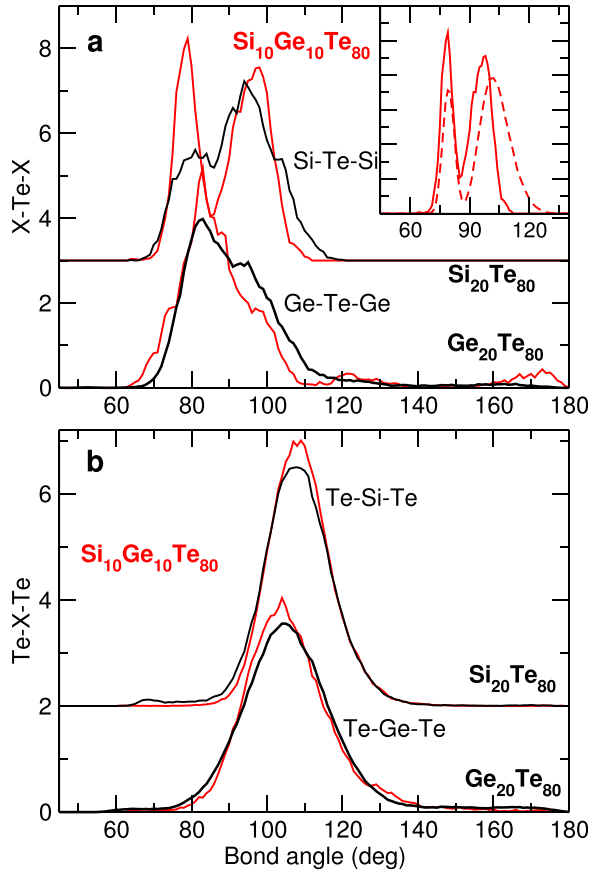

FIG. 7. Computed X-Te-X (a) and Te-X-Te (b) bond angle distribution of $Si_{20}Te_{80}$, and $Ge_{20}Te_{80}$ (black lines) at 300 K, compared to corresponding results in $Si_{10}Ge_{10}Te_{80}$ (red curves). The inset shows the Si-Te-Si bond angle distribution of $Si_{10}Ge_{10}Te_{80}$ (same as panel a), and is compared to a reference compound $Ge_{20}Se_{80}$ (Ge-Se-Ge, broken line[93]).

same situation holds for the corresponding Te-Ge-Te distribution, which is found to be very similar in both Ge-based systems, $Ge_{20}Te_{80}$ and $Si_{10}Ge_{10}Te_{80}$. Here, it is seen, however, that the Ge atom is obtained in both tetrahedral and defect octahedral (or pyramidal) sites because the distribution Te-Ge-Te is centered at angles, which are now smaller than the tetrahedral one, typically 104°. Furthermore, the small tail obtained at ≃160° is also an indication for the presence of such octahedral geometries as discussed before.[97–99] Given the width of the Te-X-Te bond angle distribution, the exact population of tetrahedral (109°) and non-tetrahedral (i.e., pyramidal, 98°) Group IV atoms cannot be estimated on a firm basis by considering the angles alone. One has to rely on an alternative approach as discussed below.

The difference between the binary systems and the ternary is substantially increased in the X-Te-X (X = Ge, Si) bond angle distribution, which shows marked changes when one considers the $Si_{10}Ge_{10}Te_{80}$ and any of the related binaries. In the ternary system, a pronounced bimodal distribution sets in (red curve in Fig. 7(a)), with two main contributions at 78° and 98°, the former being identified with ES connections between Si local geometries. This observation connects back to the conclusions made from the pair correlation function g_{SiSi}, which shows three typical peaks indicative of homopolar, ES, and CS connections in very much the same fashion as for $Ge_{20}Se_{80}$, which also give rise to a bimodal distribution[93] for the bond-angle distribution Ge-Se-Ge (inset of Fig. 7(a)). In the ternary glass, it can be observed furthermore that the separation of the ES contribution (which reduces to a shoulder of the main peak in $Si_{20}Te_{80}$) is actually related with the features detected in the partial g_{SiSi} (Fig. 5) at a distance of 3.3–3.45 Å. Consistently, the ES peak at 3.33 Å in $Si_{10}Ge_{10}Te_{80}$ is found, indeed, to separate from the main peak at 3.89 Å corresponding to CS connections. This situation contrasts with the one found for the related binary system ($Si_{20}Te_{80}$), which displays a smaller separation between the ES and CS distances (3.48 Å and 3.89 Å), and a weaker ES contribution in the Si-Te-Si bond angle distribution. Finally, it is found that in $Si_{10}Ge_{10}Te_{80}$, the main peak of the X-Te-X distribution is shifted from ≃98° to ≃82° between Si-Te-Si and Ge-Te-Ge. This obviously means that the Te atom can have two different angular environments, depending on the neighboring atoms, Ge or Si.

D. Tetrahedral fraction from constraints

A global bond-angle distribution Te-X-Te (X = Ge, Si) does not permit a precise idea about the fraction of tetrahedra present in the glasses. In Ge-Te binary systems, Akola and Jones[100] have assigned tetrahedral character, if all Ge-centered bond angles are larger than 100° but this must obviously give rise to some uncertainties given that the corresponding typical bond angles involved in the two geometries (90° and 109°) are very close (see, e.g., Fig. 7(b)), and display rather large distributions leading to a possible overlap. Alternatively, Raty and co-workers[101] use a bond-length argument in $Ge_1Sb_2Te_4$ by remarking that the fourth neighbor distribution of a central Ge atom is bimodal, and can be associated with either three- or four-coordinated (tetrahedral) Ge. On the same issue of the tetrahedral estimate, Caravati *et al.*[102] calculate a local order orientational order parameter distribution that reveals tetrahedral character[103] but the integration of this distribution, which yields the estimate, depends unfortunately on the integration boundaries. More recently, fingerprints for the presence of tetrahedral motifs have been reported in phase change tellurides from either simulated Raman spectra[104] or X-ray Absorption Near Edge Structure spectroscopy.[105]

In order to calculate quantitatively the fraction and the nature of the tetrahedra present in the glasses, we use a different approach that builds on constraint counting algorithms in combination with FPMD simulations.[56–58] Rather than considering the typical octahedral and tetrahedral angles, which are too close, we analyze the angular excursions around a central atom. In doing so, we have in mind that a tetrahedron is defined by six rigid angles or $n_c^{BB} = (2r - 3) = 5$ independent constraints[17,38] (the sixth angle is determined from the five independent ones). Over the simulation trajectory and having defined a set of N neighbors around a central Ge/Si atom, each of the $N_a = N(N-1)/2$ angles is then followed individually.[58] This defines a bond-angle distribution $P(\theta)$, which can be characterized by a mean $\bar{\theta}$ and a standard deviation σ_θ, which represents the second moment of $P(\theta)$.

If the number of low standard deviations σ_θ around an atom is six, one will detect the six rigid angles and identify a Ge/Si tetrahedron. This analysis is then performed over the whole system, and then leads to system averages and a precise fraction η_T of tetrahedra for the considered glass. Figure 8 shows the results of such an analysis by representing the system averaged Ge standard deviation $\langle\sigma_\theta\rangle$ for amorphous $Si_{10}Ge_{10}Te_{80}$. A certain number of Ge atoms display, indeed, six low standard deviations (blue bars, $_1Ge_2$, $_1Ge_3$, $_1Ge_4$, $\ldots_3Ge_4$) with $\langle\sigma_\theta\rangle \simeq 10°$, i.e., much lower than the other values resulting from angles involving the 5th and the 6th neighbor of the Ge atom (e.g., angle numbers 4, 5, 8, 9, …), which have a $\langle\sigma_\theta\rangle$ about four times larger. Once the six angular excursions are identified, Figure 8(b) shows indeed that the associated system-averaged mean angle is equal to $\langle\bar{\theta}\rangle \simeq 109°$ (blue arrows), and a corresponding bond angle distribution (Fig. 9) peaks at 109°. Both Si-centred and Ge-centred distribution are similar, and are found to be close to the corresponding Se-Ge-Se distribution[93] in the isochemical $Ge_{20}Se_{80}$ for which $\eta_T = 100\%$.

In the ternary system, the remaining non-tetrahedral (nT) Ge and Si atoms are found to have only three rigid angles (red bars) and do not have a well-defined average angle $\langle\bar{\theta}\rangle$ (Fig. 8(b)). This situation contrasts with the $Ge_{20}Te_{80}$ glass, which exhibits three angles at $\simeq 98°$ (red arrows and broken line in Fig. 8(b)), a value close to the one defining the pyramidal angle obtained[94] in amorphous As_2Se_3. In fact, an inspection of the resulting bond angle distributions (Fig. 9) shows that the Ge(nT) distribution is very close to the one found for As_2Se_3.

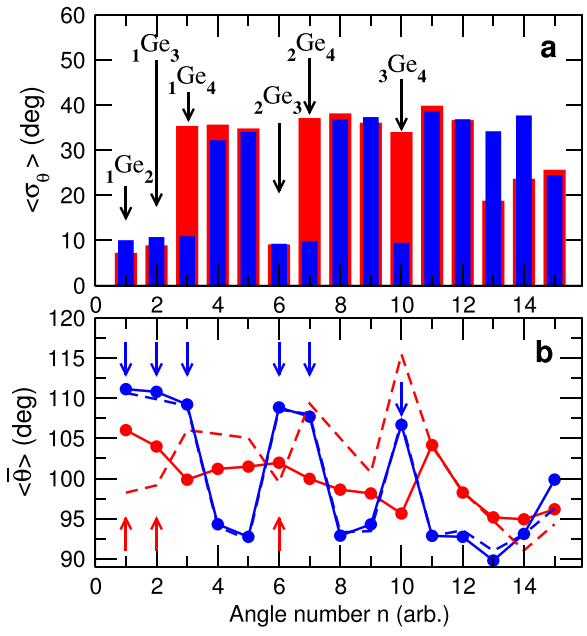

FIG. 8. (a) Standard deviation $\langle\sigma_\theta\rangle$ for arbitrary angle numbers n ($0 < n < N_a = 15$) around Ge atoms in amorphous $Si_{10}Ge_{10}Te_{80}$ are split into two categories: Ge atoms having 6 low σ_θ's (blue), and Ge atoms having not such σ_θ's (red). The arrows indicate the relevant angles $_kGe_m$(n) serving for the discussion. Here, m and $k < m$ are the Te neighbors, and labelled according to their distance with respect to the central Si atom. (b) Corresponding Ge-centred angles $\langle\bar{\theta}\rangle$. The broken lines correspond to the results for $Ge_{20}Te_{80}$. Blue colored arrows indicate angles, which can be considered as rigid (because of panel (a)) and these correspond to tetrahedral local geometry.

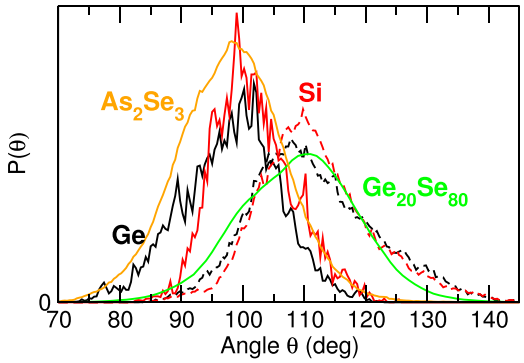

FIG. 9. Bond angle distribution of identified Ge (black) and Si (red) tetrahedral (T, broken lines)/non-tetrahedral (nT, solid lines) in amorphous $Si_{10}Ge_{10}Te_{80}$ according to the constraint analysis of Fig. 8. Reference curves are shown for the Se-Ge-Se bond angle distribution in the isovalent $Ge_{20}Se_{80}$ having 100% tetrahera[93] (green curve), and for the Se-As-Se bond angle distribution[94] in As_2Se_3 (orange curve), which has a nearly 100% pyramidal geometry.

Finally, we estimate from the count of Ge atoms fulfilling the condition of six rigid constraints the fraction of tetrahedra in amorphous $Si_{10}Ge_{10}Te_{80}$, and find $\eta_T = 33.67\%$. Here, Si sites contribute to 42.74% and Ge sites to 24.6%. These values are lower than those determined for the related binary systems: 54.6% for $Ge_{20}Te_{80}$ and 91.8% for $Si_{20}Te_{80}$. It should, finally, be also noted that a $Ge_{20}Te_{80}$ system without the Grimme correction taking into account the dispersion forces lead to systems, which contain less Ge tetrahedra as one finds $\eta_T = 38.2\%$. The difference with the computed $\eta_T = 54.6\%$ may arise from bond lengths, which are reduced when Eq. (2) is used, which promotes an increased tetrahedral bonding, a feature quite well established for various glass-forming systems, especially when a tetrahedral to octahedral conversion is followed under pressure.[106]

E. Tetrahedral fraction from Mössbauer spectroscopy

We compare the findings on the computed tetrahedral fraction η_T with results from ^{119}Sn Mössbauer spectroscopic studies conducted on $Ge_xSi_xTe_{1-2x}$ glasses to probe the local chemistry of Ge and Si. Here, traces ($\simeq$1 at. %) of ^{119}Sn have been doped into the glass of interest by reacting isotopically enriched elemental ^{119}Sn. There is overwhelming evidence that when Sn is doped in dilute amounts, it replaces isovalent Si and Ge local environments in the network, and reproduces their local geometry and chemical bonding.[107] For the analysis, it is useful to first identify spectra of several standard compounds having a well-defined valence. When Sn is in a tetrahedral sp^3-bonded state as a dilute substituent in c-Si, one observes a sharp Mössbauer resonance with unique chemical shift of $\delta = 1.65 \pm 0.02$ mm/s with respect to Sn^{4+} as in $BaSnO_3$ (Fig. 10), this shift being characteristic of tetrahedrally coordinated Sn. Similarly, the Sn^{2+} oxidation state is found in crystalline SnTe, which has an octahedral geometry as in GeTe,[108] as revealed by a Mössbauer resonance at an isomer shift of $\delta = 3.33 \pm 0.02$ mm/s. Furthermore, since there are no vacancies in this perfect rocksalt-type structure of two Sn- and Te-sublattices,[108] no quadrupole splitting is observed,[109] which indicates neither a

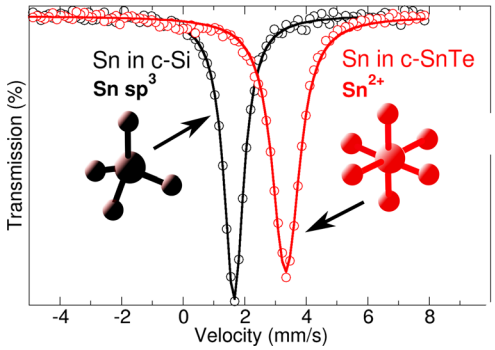

FIG. 10. ^{119}Sn Mössbauer spectra of Sn in c-Si (black) and c-SnTe (red). Note that a resonance is observed at $\delta = 1.65 \pm 0.02$ mm/s when Sn is tetrahedrally coordinated, and $\delta = 3.33 \pm 0.02$ mm/s when Sn is octahedrally coordinated.

distorted octahedra nor the presence of vacancies in the immediate environment.

Fig. 11 shows the Mössbauer effect observed in the ternary $Ge_xSi_xTe_{1-2x}$ glasses at selected compositions. Each line shape can be deconvoluted into a singlet (denoted by "T") centered at around $\delta_T \simeq 1.95$ mm/s and a doublet (denoted by "DO") in the $\delta_{DO} \simeq 3.19$ mm/s to 3.27 mm/s range. When the spectra are compared to the reference compounds of Fig. 10, it becomes clear that the resonance at δ_T can be identified with tetrahedral (T) sites, whereas the resonance at δ_{DO} is obviously linked with the non-tetrahedral sites. Furthermore, as the DO resonance exhibits a doublet with a quadrupole splitting Δ, we are observing a defect octahedral (DO) site displaying an electric field gradient,[109] i.e., the local pyramidal geometry, which has been previously detected from the angular excursions (Fig. 8).

An inspection of the effect of the composition shows that the DO resonance peak integrated intensity increases with cross-linking concentration x, and exceeds that of the singlet (T) resonance for $Si_{10}Ge_{10}Te_{80}$ (Fig. 11(c)). We find the asymmetry of the doublet at δ_{DO} also increases progressively. A Lorentzian fit of the lineshape provides the parameters (Table II), and, ultimately, one obtains the fraction η_T^{exp} (integrated intensity) of Sn being at tetrahedral sites.

One notes that the fraction η_T^{exp} of tetrahedral sites decreases dramatically (from $\simeq$80% to 40%, Table II) within a few percent change, i.e., from $Si_6Ge_6Te_{88}$ to $Si_{10}Ge_{10}Te_{80}$, underscoring major structural changes in the network with a rapid conversion of Ge/Si tetrahedra into defect-octahedral (pyramidal) geometries. Between 6% and 10% range, the rate of change in tetrahedra is about 9.8% per atomic percent (%) composition. A linear extrapolation indicates that η_T^{exp} may be nearly 100% at $Si_4Ge_4Te_{92}$. Although one cannot access the Si versus Ge fraction of tetrahedra, one notes that the total measured integrated intensity $\eta_T^{exp} = 40.8\%$ compares rather well with the calculated fraction $\eta_T = 33.7\%$ obtained for the simulated model of $Si_{10}Ge_{10}Te_{80}$ (Sec. III D).

IV. EXPERIMENTAL RESULTS

We now turn to the experimental results permitting the detection of rigidity transitions, and show that the present

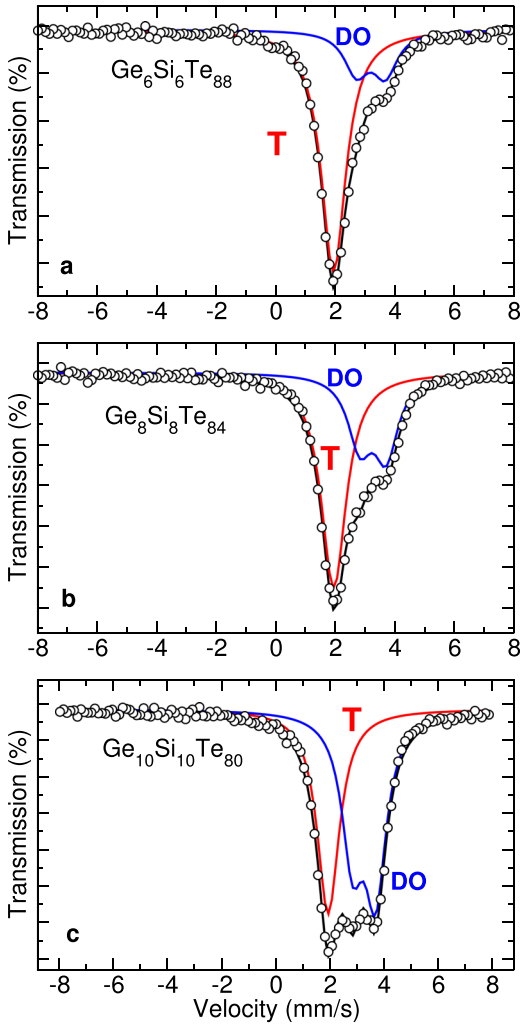

FIG. 11. ^{119}Sn Mössbauer spectra of $Ge_xSi_xTe_{100-2x}$ ternary glasses for selected compositions. Deconvolution into tetrahedral (T, red) and defect-octahedral (DO, blue).

investigated tellurides display the same phenomenology as many other reported chalcogenide and oxide glasses.

A. Scanning calorimetry measurements

Fig. 12(a) shows the non-reversing enthalpy (ΔH_{nr}) variation of the $Ge_xSi_xTe_{100-2x}$ glasses as a function of composition x. It is useful to remind that after synthesis, all samples were T_g cycled by heating above T_g at a scan rate of 3 °C/min followed by a cooling down at the same scan rate. From Fig. 12, it can be seen that the ΔH_{nr} variation shows a broad global minimum centered at $x \simeq 8\%$ after reacting starting materials for 7 days followed by a steady increase until $x = 12\%$ and a reduction after $x > 12\%$. In addition, the effect of stress removal can be observed. The non-reversing enthalpy variation of $Si_xGe_xTe_{1-2x}$ measured soon after T_g cycling (red curve, Fig. 12(a)) and after aging for 2 months (blue curve) shows, indeed, that the ΔH_{nr} term remains nearly unchanged in $7.5\% < x < 9\%$ range. As T_g cycling is performed soon after sample synthesis to remove stress that may have frozen in due to the quenching process, one thus realizes that for this particular window in composition, glass must display a minimum stress.

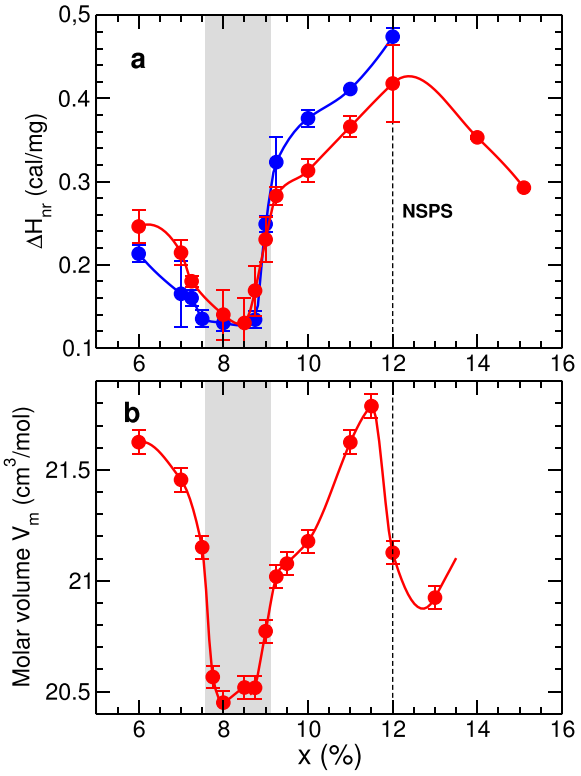

FIG. 12. (a) Non-reversing heat flow ΔH_{nr} of $Si_xGe_xTe_{1-2x}$ ternary glasses as a function of composition x. The red curve is a measurement after rejuvenation (T_g cycling), whereas the blue curve is a measurement after an ageing time of 2 months. (b) Molar volume V_m as a function of composition x. The gray zone indicates the compositional range, where both quantities obviously minimize, and which can be identified with a stress-free IP. The maximum observed around 12% can be associated with a nanoscale phase separation (NSPS, see text for details).

TABLE II. Measured fraction η_T^{exp} of tetrahedra, and parameters from Mössbauer spectroscopy for the identified tetrahedral (T) and defect octahedral (DO, pyramidal) resonance peaks. Isomer shift δ, quadrupole splitting Δ (for DO geometry), and full width at half maximum (FWHM) in $Si_xGe_xTe_{1-2x}$ glasses with changing content.

		$Si_6Ge_6Te_{88}$	$Si_8Ge_8Te_{84}$	$Si_{10}Ge_{10}Te_{80}$
η_T^{exp}(%)		79.9	60.7	40.8
δ(mm/s)	T	1.95	1.95	1.93
	DO	3.19	3.27	3.25
Δ (mm/s)		0.78	0.85	0.73
FWHM (mm/s)	T	1.00	1.02	1.00
	DO	0.98	0.97	0.96

Fig. 12(b) shows the molar volume measurements of the $Si_xGe_xTe_{1-2x}$ ternary glasses, and it is found that molar volumes display an abrupt decrease in the same region as ΔH_{nr} ($7.5\% < x < 9\%$), and plateaus out until $x \simeq 9\%$. The important increase in V_m observed in the $9\% < x < 11.5\%$ range is followed by a sharp decrease thereafter. It should be noted that within a percent composition change, the variation in molar volume is quite important, about 5%–6% close to the $x \simeq 7.5$ %.

Given that both quantities usually serve as signatures[79,80] for the onset of rigidity, both trends in $Si_xGe_xTe_{1-2x}$ (Fig. 12) indicate that a flexible to rigid transition is achieved by the addition of Ge/Si cross-links into a Te-rich amorphous network structure. Furthermore, a stress-free IP is observed (gray zone) in the $7.5\% < x < 9\%$ range. We discuss its origin in Sec. V.

B. Fragility

Figure 13(a) shows the in-phase ($Re(C_p^*)$) and out-of-phase C_p ($Im(C_p^*)$) signals measured for the x = 6% sample of $Si_xGe_xTe_{1-2x}$ ternary at several modulation frequencies. In-phase C_p signal shows a step near the glass transition, while the out-of-phase C_p ($Im(C_p^*)$) shows a characteristic endothermic peak near T_g. Both the step and the endothermic peak shift to higher temperatures as the modulation frequency (ω) is increased. The location of the peak in $Im(C_p)$ and the modulation frequency ω allow obtaining the relaxation time (τ) of the supercooled liquid given that one has $\omega\tau = 1$ at the peak maximum of $Im(C_p)$. From the temperature dependence of τ in an Angell plot,[113] and using Eq. (1), one then extracts the fragility index $\mathcal{M}$ as a function of composition.

Fig. 13(b) shows this fragility index variation in $Ge_xSi_xTe_{100-2x}$ glasses as a function of x. $\mathcal{M}$ values initially decrease as x is increased and shows a global minimum centered at $x = 8.5\%$ with a minimum value of $\mathcal{M} = 26$. This minimum is obtained in the IP range, similarly to previous investigations on selenides and sulfides.[23,113–115]

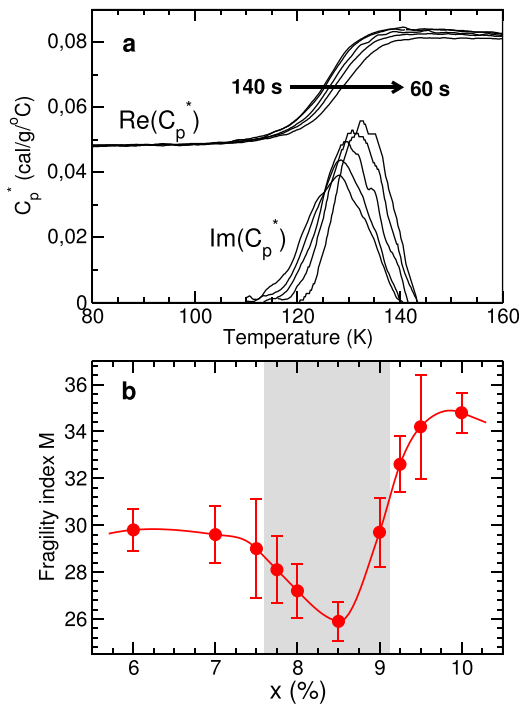

FIG. 13. (a) In-Phase (real) and Out-of-Phase (imaginary) parts of the complex heat capacity C_p^* for a $Si_6Ge_6Te_{88}$ glass were obtained from MDSC measurements at a rate of 3 °C/min and a modulation amplitude of 1 °C over five periods (1 °C/60 s, 80 s, 100 s, 120 s, 140 s). (b) Fragility index values $\mathcal{M}$ of the present $Si_xGe_xTe_{1-2x}$ ternary system as a function of composition x.

V. DISCUSSION

Having in hand both the theoretical and experimental results, we can now discuss the general behavior of the effect of the addition of Ge/Si cross-links on the physical properties of amorphous telluride networks.

A. Identification of rigidity transitions

1. Rigidity transitions from the experimental data

There is a striking correlation in the variation of ΔH_{nr} and that of molar volume V_m in composition $x_{c1} = 7.5\% < x < 9\% = x_{c2}$ range, where a global minimum in ΔH_{nr} is found to coincide with that in molar volumes. The behavior is characteristic of intermediate phases, where compacted networks form, i.e., molar volumes show a global minimum.[4,79,80,114,117] Small aging[110–112] (as compared to outside of the IP window) of glasses in this special phase stems from the stress-free character of the network as demonstrated from Raman pressure experiments in selenide glasses.[118]

Given the way, the Ge/Si cross-links are added into the base Te network, one is led to believe that at low $x < 7.5\%$, glasses are flexible and should be underconstrained ($n_c < 3$). Since an increase in T_g is observed, and since it is well established that the glass transition temperature variation is a measure of network connectivity,[73,119] one can conclude that the average coordination number will increase with composition x, leading to an increased stiffening of the network until the glass becomes rigid at $x = x_{c1} \simeq 7.5\%$. Over the IP compositional window $\Delta x = x_{c2} - x_{c1}$, obviously, small changes in V_m and ΔH_{nr} are obtained (Fig. 12), defining a nearly square well behavior with composition. As the cross-link density continues to increase, these networks become stressed rigid when the Ge/Si concentration becomes larger than $x = x_{c2} \simeq 9\%$, and both ΔH_{nr} and V_m increase in a dramatic fashion for $x > x_{c2}$.

In addition, we remark that the location of the minimum in fragility $\mathcal{M}$ at $x \simeq 8.5\%$ is found inside the obtained window Δx from molar volume and non-reversing heat flow measurements (Fig. 13). This feature is also a strong argument in favour of the stress-free IP given that the correlation between calorimetric, volumetric, and fragility anomalies for IP compositions has been found for other network glass-forming systems such as Ge_xSe_{1-x},[113] As_xSe_{1-x},[114] $As_xGe_xSe_{1-2x}$,[26,115] (Fig. 14). In contrast with the lighter chalcogenides, which exhibit a very low fragility ($\mathcal{M} \simeq 15$) in the IP window[113] and lead to strong glass-forming liquids; here, the obtained fragilities for $Si_xGe_xTe_{1-2x}$ are much higher, including at the minimum (8.5%), where $\mathcal{M} \simeq 26$. Broadly speaking, variations of $\mathcal{M}(x)$ in present tellurides are smaller as compared to, e.g., Ge_xSe_{1-x} melts,[113] which display larger variations of $\mathcal{M}$ across the flexible and stressed rigid phases. An explicit relationship between enthalpic changes at the glass transition and the fragility has, furthermore, been established[120] from a Kirkwood-Keating model of network glasses, showing that the activation energy for relaxation (or the fragility) is proportional to the enthalpic changes at the glass transition, and *minimize* at an isostatic ($n_c = 3$) composition, where rigidity onsets.

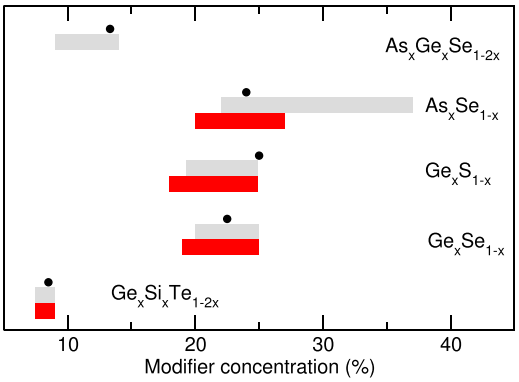

FIG. 14. Location of fragility minima (filled circles) in chalcogenide network glasses, compared to the location of the non-reversing heat flow windows ΔH_{nr} (gray) and to the volumetric windows indicating space-filling tendency (red): present $Si_xGe_xTe_{1-2x}$, Ge_xSe_{1-x},[113] Ge_xS_{1-x},[23] As_xSe_{1-x},[114] $As_xGe_xSe_{1-2x}$.[26,115]

2. Comparison with previous findings

The detection of an IP is consistent with results reported by Asokan *et al.*[47,48,62–64,71] on a slightly different compositional join ($Si_xGe_{15}Te_{85-x}$, Figure 15), which also exhibit either minima of the non-reversing heat flow ΔH_{nr}, or anomalies in molar volume, and thermal stability $\Delta T = T_x - T_g$ maximizing. On the mechanical properties, these authors notice that the elastic modulus and the hardness are substantially increased and display a threshold behavior, once the system becomes stressed rigid,[67] similarly to what has been obtained under pressure.[34] For lower connectivities, both mechanical properties saturate in the IP as the network is adapting to maintain a nearly isostatic character.

3. Rigidity transitions from MD based constraint counting

In the $Si_xGe_{15}Te_{85-x}$ system, identification of the mean-field rigidity transition has been established[65,67] from the 8-$\mathcal{N}$ bonding rule (Fig. 15). However, the latter does not take into account the fact that both T and DO-pyramidal geometries are present, and that they do not involve the same

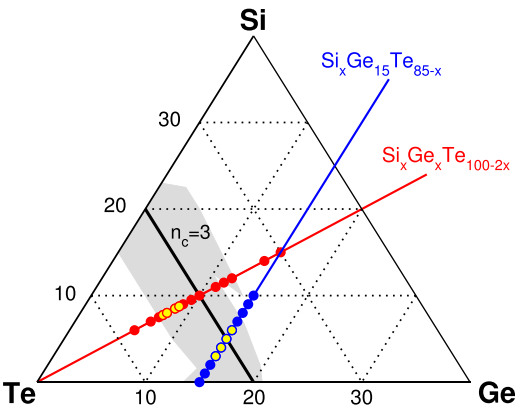

FIG. 15. GFR of Si-Ge-Te glasses from Feltz *et al.*[60] (gray zone), presently studied ternary compositions (red), and the ternary compositions $Ge_{15}Si_xTe_{85-x}$ studied by Asokan and co-workers[65] (blue). The yellow points represent the IP compositions, and the thick black line represents the $GeTe_4$-$SiTe_4$ join fulfilling the mean-field rigidity transition ($n_c = 3$), if a 8-$\mathcal{N}$ bonding rule is assumed.

number of angular constraints (Fig. 8). We can calculate a mean-field constraints count per atom by using the definition[17,18]

$$n_c = \frac{\sum_{r\geq 2} n_r \left[\frac{r}{2} + 2r - 3\right]}{\sum_{r\geq 2} n_r}, \quad (7)$$

where n_r is the concentration of an r-fold atom. We combine the FPMD obtained structural model with constraint counting based on radial and angular excursions, following a framework established and validated previously.[56–58] Based on the previous analysis, we assume that Ge and Si are four-fold coordinated (Table I) and are found in both tetrahedral and pyramidal-DO geometry, the population of the former being characterized by the fractions η_T^{Si} and η_T^{Ge}. The analysis from the angular standard deviation σ_θ (Fig. 8) but also previous enumerations[14–16] show that 5 and 3 BB constraints can be associated with a T and a DO geometry, respectively. It is assumed that Te has a coordination number $r_{Te} > 2$, consistent with our FPMD calculation ($r_{Te} = 2.39$). The fact that tellurium deviates from the anticipated 8-$\mathcal{N}$ bonding rule (see, however, Ref. 68), and has $r_{Te} > 2$ should give rise to additional BS ($r_{Te}/2$) and BB constraints. However, an inspection of the excursions (characterized by the standard deviation σ_θ of the distribution) of the angles defined by the first three neighbors of a Te atom show that only the angle defined by the first two neighbors is relevant. Indeed, such an angle has a small angular excursion, which leads to a sharp distribution for the angular standard deviation (Fig. 16), centered at small $\sigma_s\theta$. This allows identifying[57] an intact BB constraint for the distribution 102, whereas other angles involving the third neighboring atom of Te obviously have ineffective angular constraints because they display a very broad distribution f(σ_θ). One, thus, has for Te, $n_c^{BS} = r_{Te}/2$, and $n_c^{BB} = 1$.

Using Eq. (7) for the $Si_xGe_xTe_{1-2x}$ alloy and the established count of constraints and local structure, we can now write the density of constraints as

$$n_c = x(5 + 2\eta_T^{Ge}) + x(5 + 2\eta_T^{Si}) + (1 - 2x)\left(1 + \frac{r_{Te}}{2}\right) \quad (8)$$

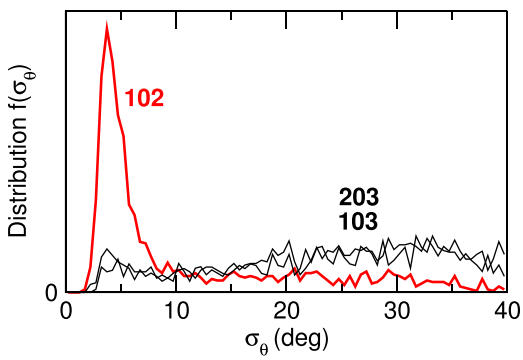

FIG. 16. Computed distribution of angular standard deviations σ_θ around a central "0" Te atom for the first two neighbors (102, red curve) and for the angles involving a third neighbor (103 and 203, black lines).

leading to

$$n_c = \left[4x + \frac{r_{Te}}{2}(1 - 2x)\right] + [1 + 4x(1 + \eta_T(x))], \quad (9)$$

where we have used $2\eta_T(x) = \eta_T^{Ge} + \eta_T^{Si}$ that can be determined from the integrated intensity of the Mössbauer resonance spectra. The two squared brackets refer to BS and BB contributions, respectively.

Although Mössbauer spectroscopy has been performed on selected (3) compositions (Table II), it is important to emphasize that the chemical bonding in the present tellurides is strongly influenced by the elastic nature of the network. In fact, the flexible composition (6%) is found to be dominated by tetrahedra underscoring a sp^3 geometry, whereas the pyramidal geometry is found to be the majority local structure for the stressed rigid composition (10%). With only three investigated compositions, we cannot further comment on the link between the tetrahedral (T) to pyramidal (DO) geometry conversion and the three elastic phases, but we stress that this feature is absent in other chalcogenides (S, Se) and may, thus, be viewed as a typical property of tellurides. In order to be somewhat more quantitative, we fit the trend in composition of η_T^{exp} (Table II) with a linear function, and use it ($\eta_T(x)$) in Eq. (9) to determine the contribution n_c^{BS} and n_c^{BB} of both BS and BB constraints with composition. Results are shown in Fig. 17, and it is found that, while the BS density is increasing with Ge/Si content due to the increased network connectedness, the contribution of BBs saturates and eventually decreases at larger compositions, originated by the T to DO conversion. We view the latter as a manifestation of *network adaptation*, a way to reduce the number of rigid constraints as the fraction of cross-links is steadily increased. Indeed, it has been stressed that tetrahedra involve five BB constraints, whereas a DO structure will involve only three (see Fig. 9). For a given fraction η_T of tetrahedra, the number of BB constraints per atom is $n_c^{BB} = 5\eta_T + 3(1 - \eta_T) = 3 + 2\eta_T$. As n_c^{BS} is increasing with the Ge/Si content, glasses can eventually adapt the increasing stress by reducing the number n_c^{BB} of angular constraints thanks to the T to DO conversion (Table II), in a fashion similar to what has been recently established from MD simulations in oxides.[116]

B. Identification of a nanoscale phase separation

The reduction of $\Delta H_{nr}(x)$ and $V_m(x)$ at $x > 12\%$ (Fig. 12) are most probably manifestations of nanoscale phase separation (NSPS) in these ternary glasses as reported previously for a large number of glasses with rather well documented features: maximum in ΔH_{nr},[23,121] anomalies in a variety of mechanical properties,[67,122] maximum in glass transition temperature.[123] This latter manifestation is actually recovered with the observation of a maximum in T_g (Fig. 1) in the present $Si_xGe_xTe_{1-2x}$ glasses. The NSPS manifests by a decoupling of Group IV atoms from the network backbone, which results in the formation of ethylene-like (ET) units such as $Se_{3/2}Ge\text{-}GeSe_{3/2}$ in Ge-Se glasses[23,121] (Fig. 6). The underlying driving force stems from the highly stressed rigid nature of the glass structure (usually $n_c \simeq 3.6$),

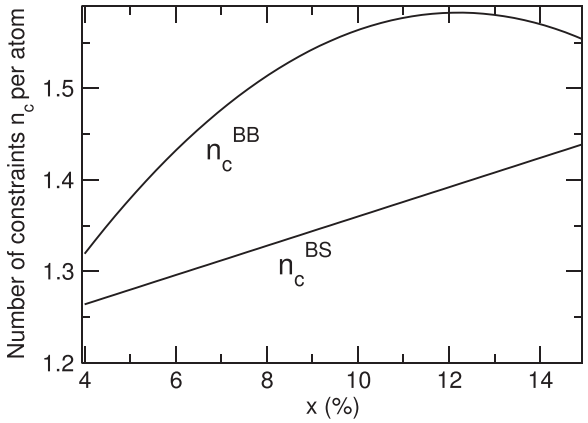

FIG. 17. Computed number of constraint n_c split into BS and BB contributions as a function of Ge/Si content x in $Si_xGe_xTe_{1-2x}$ glasses, assuming a Te coordination number of $r_{Te}=2.4$, and an evolution of tetrahedral fraction $\eta_T(x)$ depending on composition following what has been determined in Table II.

which is then unable to maintain homogeneity under the action of a too large number of bending and stretching interactions so that a phase separation at the nanoscale is preferred. Upon further addition of Group IV atoms, this NSPS will hold, but one then reaches the limit of the GFR.

The observation of a nanoscale phase separation deserves an additional comment. It has been stressed, indeed, that the anomaly (i.e., the observed maxima that we associate with NSPS) is simply the result of a chemical threshold.[124] This statement has been made from the observation that in Ge-Se and Ge-S alloys, the maxima are located close to the stoichiometric compositions of 33% Ge associated with the existing crystalline polymorphs $GeSe_2$ (Ref. 125) and GeS_2.[126] However, the results on the $Si_xGe_xTe_{1-2x}$ glasses do not support this view. In fact, the anomaly is obtained at $x \simeq 12\%$, which does not correspond to any reported crystalline polymorph for the ternary nor for the related binary alloys given that only GeTe (Ref. 108) (50% Ge) and Si_2Te_3 (Ref. 96) (40%) are the known crystalline phases. The possibility of a chemical threshold is also contradicted by the behavior with composition of other Si based alloys (e.g., Si-Se (Ref. 69)), which do, indeed, have a crystalline compound[127] $SiSe_2$ but which do not exhibit any anomaly in T_g or $\Delta H_{nr.}$.[69] Raman spectroscopy[69] and FPMD simulations[128] indicate the absence of homopolar Si-Si bonds, consistent with our claim that NSPS maximum in T_g and presence of homopolar (ET, Fig. 6) bonds are correlated.

In the present Si-Ge-Te ternary system, it would be interesting to test such conclusions using molecular simulations, and follow the fraction of, e.g., ET units or the population of homopolar Ge-Ge and Si-Si bonds and as a function of composition.[93] Given the size of the system (200 atoms), such a study is unfortunately beyond the scope of the paper. We note however from Fig. 5 that Ge-Ge and Si-Si bonds do exist in the structure for $x=10\%$, and at a fraction, which is larger than in the corresponding binary Ge-Te and Si-Te alloys.

VI. CONCLUDING REMARKS

Group IV atoms in a base Te-rich network leads to the formation of glasses in a limited range of composition for the $Si_xGe_xTe_{1-2x}$, in contrast with selenides and sulfides. The glass-forming region is found between $x=6\%$ and $x=15\%$, and consistent with previous investigations on this system.[60,65] Here, we have combined an experimental probe with a theoretical study to investigate the effect of cross-linking on the Te network. FPMD simulations of a selected composition ($Si_{10}Ge_{10}Te_{80}$) are performed and compared to the parent binary alloys $Ge_{20}Te_{80}$ and $Si_{20}Te_{80}$. Results show that the structure of the ternary compound is very close to those on the binary $Si_{20}Te_{80}$ as revealed from the calculation of the total structure factor $S_T(k)$ and the pair correlation function $g(r)$. An increased tendency to form edge-sharing units is found in the ternary glass, detected from a typical distance in the partial $g_{SiSi}(r)$ and the bond angle distribution Si-Te-Si. We introduce a method allowing for the computation of the fraction of tetrahedra in sp^3 geometry, and find that fraction (33.67%) to be lowered in the ternary glass, but in excellent agreement with the experimental estimate (40.8%). The latter was deduced from the integrated intensity of Mössbauer resonance spectra, which display two characteristic sites, one associated with the tetrahedral geometry and the other with a defect octahedral (pyramidal) one. The simulations allow one to calculate the contribution of the two species (Ge, Si), and it is found that there are nearly twice Si tetrahedra more (42.74%) than Ge ones (24.6%). When followed with composition, it is found that the experimental fraction of tetrahedra decreases with Ge/Si content, a trend that we associate with *angular adaptation*, similarly to what has been found in rigidity transitions driven by pressure.[116]

We then investigated the possibility of elastic phases and rigidity transitions in this ternary glass, similar to what has been successfully reported for a number of chalcogenides. We found that the addition of the Ge/Si cross-links leads to a global stiffening of the Te-rich network, which undergoes two separate transitions defining an intermediate phase: a flexible to rigid transition at $x_{c1}=7.5\%$ and a rigid to stressed rigid transition at $x_{c2}=9\%$, both being defined by an abrupt variation in molar volume and non-reversing enthalpy. In the intermediate phase, the corresponding glass-forming melts are, furthermore, found to display a fragility minimum, which implies that the present IP telluride melts have a more stronger behavior than glass-forming melts in the flexible and stressed rigid phase. We use the structural model obtained from FPMD to establish the exact number of constraints n_c, knowing that (i) not all Group IV atoms are in sp^3 geometry, and (ii) an increased coordination number for the tellurium atom has to be taken into account. Finally, we identified a nanoscale phase separation in these ternary Si-Ge-Te glasses, which leads to a maximum in glass transition temperature, molar volume and non-reversing heat flow, and precedes the limit of the glass-forming region. This separation is independently revealed from a pronounced first peak in the calculated pair correlation function $g_{GeGe}(r)$, associated with homopolar Ge-Ge bonds.

Given the technological importance of amorphous tellurides, the discovery of an IP (see also Fig. 14) in the present system indicates that a certain number of promising applications can be considered using the standard IP

properties. For instance, it is well known that retention loss of the amorphous phase is a key reliability issue of phase change material devices,[8] which stems from the instability of the non-equilibrium amorphous phase due to the evolution of the physical properties with time. The existence of an IP in $Si_xGe_xTe_{1-2x}$ demonstrates that such phases are generic, i.e., they are not peculiar to Selenides or Sulfides, but also exist in Tellurides. The weaker relaxation in IPs may be utilized in PCM to stabilize device performance. The smaller aging behavior of the ΔH_{nr} term is, indeed, a clear indication of the stability of glassy compositions in the $7.5\% < x < 9\%$ range. This result suggests that atoms change their configuration minimally over time, and may thus maintain important PCM properties such as resistivity or optical contrast nearly unchanged.

ACKNOWLEDGMENTS

M.M. acknowledges support from Agence Nationale de la Recherche (ANR) (Grant No. ANR-11-BS08-0012), from the Franco-American Fulbright Commission, and International Materials Institute (H. Jain). P.B. acknowledges support from NSF Grant No. DMR-08-53957. Mathieu Bauchy and Daniel Skończ-Traintz are gratefully acknowledged for stimulating discussions. It is a pleasure to thank Stave Hall and Lexie Niemoeller for discussions on modulated DSC measurements.

[1]In *Glass Science and Technology*, edited by D. R. Uhlmann and N. J. Kreidl (Academic Press, New York, 1986).
[2]M. A. Popescu, *Non-Crystalline Chalcogenides* (Kluwer Academic, New York, 2000).
[3]Z. Borizova, *Glassy Semiconductors* (Plenum Press, New York, London, 1981).
[4]K. Shimakawa, A. Kolobov, and S. R. Elliott, Adv. Phys. **44**, 475 (1995).
[5]J. Troles, V. Shiryaev, M. Churbanov, P. Houizot, L. Brilland, F. Desevedavy, F. Charpentier, T. Pain, G. Snopatin, and J. L. Adam, Opt. Mater. **32**, 212 (2009).
[6]J. Keirsse, C. Boussard-Plénel, O. Loréal, O. Sire, B. Bureau, P. Leroyer, B. Turlin, and J. Lucas, J. Non-Cryst. Solids **326–327**, 430 (2003).
[7]M. Wuttig, Nature Mater. **4**, 265 (2005).
[8]In *Phase Change Materials and Applications*, edited by S. Raoux and M. Wuttig (Springer, Berlin, 2008).
[9]A. V. Kolobov, P. Fons, A. I. Frenkel, A. L. Ankudinov, J. Tominaga, and T. Uruga, Nature Mater. **3**, 703 (2004).
[10]S. R. Elliott, *Physics of Amorphous Materials* (Longman Scientific Technical Press, New York, 1990).
[11]A. Wilhelm, C. Boussard-Plédel, Q. Coulombier, J. Lucas, B. Bureau, and P. Lucas, Adv. Mater. **19**, 3796 (2007).
[12]V. S. Shiryaev, J. L. Adam, X. H. Zhang, C. Boussard-Plédel, J. Lucas, and M. F. Churbanov, J. Non-Cryst. Solids **336**, 113 (2004).
[13]C. Vigreux-Bercovici, E. Bonhomme, A. Pradel, J. E. Broquin, L. Labadie, and P. Kern, Appl. Phys. Lett. **90**, 011110 (2007).
[14]In *Rigidity Theory and Applications*, edited by M. F. Thorpe and P. M. Duxbury (Kluwer Academic, Plenum Publishers, New York, 1999).
[15]In *Rigidity and Boolchand Intermediate Phases in Nanomaterials*, edited by M. Micoulaut and M. Popescu (INOE Publishing House, Bucarest, 2009).
[16]In *Insulating and Semi-conducting Glasses*, edited by P. Boolchand (World Scientific, Singapore, 2000).
[17]M. F. Thorpe, J. Non-Cryst. Solids **57**, 355 (1983).
[18]H. He and M. F. Thorpe, Phys. Rev. Lett. **54**, 2107 (1985).
[19]J. D. Musgraves, P. Wachtel, B. Gleason, and K. Richardson, J. Non-Cryst. Solids **386**, 61 (2014).
[20]Y. Wang, M. Nakamura, O. matsuda, and K. Murase, J. Non-Cryst. Solids **266–269**, 872 (2000).
[21]P. Chen, C. Holbrook, P. Boolchand, D. G. Georgiev, and M. Micoulaut, Phys. Rev. B **78**, 224208 (2008).
[22]Z. G. Ivanova, V. S. Vassilev, S. V. Boychava, and N. Kirov, J. Non-Cryst. Solids **232–234**, 274 (1998).
[23]S. Chakraborty and P. Boolchand, J. Phys. Chem. B **118**, 2249 (2014).
[24]A. Feltz, H. Aust, and A. Blayer, J. Non-Cryst. Solids **55**, 179 (1983).
[25]J. Y. Duquesne and G. Bellassa, J. Phys. Colloq. **46**, C10 (1985).
[26]Y. Wang, P. Boolchand, and M. Micoulaut, Europhys. Lett. **52**, 633 (2000).
[27]E. L. Gjersing, S. Sen, and B. Aitken, J. Phys. Chem. C **114**, 8601 (2010).
[28]R. A. Bohmer and C. A. Angell, Phys. Rev. B **45**, 10091 (1992).
[29]Y. Vaills, T. Qu, M. Micoulaut, F. Chaimbault, and P. Boolchand, J. Phys. Condens. Mater. **17**, 4889 (2005).
[30]B. P. Rodrigues and L. Wondraczek, J. Chem. Phys. **138**, 244507 (2013).
[31]D. Novita, P. Boolchand, M. Malki, and M. Micoulaut, Phys. Rev. Lett. **98**, 195501 (2007).
[32]K. Trachenko, M. T. Dove, V. Brazhkin, and F. S. El'kin, Phys. Rev. Lett. **93**, 135502 (2004).
[33]M. Malki, M. Micoulaut, F. Chaimbault, and Y. Vaills, Phys. Rev. Lett. **96**, 145504 (2006).
[34]M. M. Smedskjaer, J. C. Mauro, and Y. Yue, Phys. Rev. Lett. **105**, 115503 (2010).
[35]M. Smedskjaer, J. C. Mauro, R. E. Youngman, C. L. Hogue, M. Potuzak, and Y. Yue, J. Phys. Chem. B **115**, 12930 (2011).
[36]J. C. Mauro and M. Smedskjaer, Physica A **391**, 6121 (2012).
[37]A. I. Fu and J. C. Mauro, J. Non-Cryst. Solids **361**, 57 (2013).
[38]J. C. Phillips, J. Non-Cryst. Solids **34**, 153 (1979).
[39]M. Micoulaut and J. C. Phillips, Phys. Rev. B **67**, 104204 (2003).
[40]W. A. Kamitakahara, R. L. Cappelletti, P. Boolchand, B. Halfpap, F. Gompf, D. A. Neumann, and H. Mutka, Phys. Rev. B **44**, 94 (1991).
[41]R. L. Cappelletti, M. Cobb, D. A. Drabold, and W. A. Kamitakahara, Phys. Rev. B **52**, 9133 (1995).
[42]J. C. Maxwell, Philos. Mag. **27**, 294 (1864).
[43]J. C. Phillips, Phys. Today **35**(2), 27 (1982).
[44]P. Tronc, M. Bensoussan, A. Brenac, and C. Sebenne, Phys. Rev. B **8**, 5947 (1973).
[45]C. Y. Fang, H. Yinnon, and D. R. Uhlmann, J. Non-Cryst. Solids **57**, 465 (1983).
[46]M. Micoulaut, Am. Mineral. **93**, 1732 (2008).
[47]B. H. Sharmila, J. T. Devaraju, and S. Asokan, J. Non-Cryst. Solids **326–327**, 154 (2003).
[48]G. Sreevidya Varma, C. Das, and S. Asokan, Solid State Commun. **177**, 108 (2014).
[49]X. Feng, W. Bresser, and P. Boolchand, Phys. Rev. Lett. **78**, 4422 (1997).
[50]A. N. Sreeram, A. K. Varshneya, and D. R. Swiler, J. Non-Cryst. Solids **128**, 294 (1991).
[51]P. Lebaudy, J. M. Saiter, J. Grenet, M. Belhadji, and C. Vautier, Mater. Sci. Eng., A **132**, 273 (1991).
[52]P. Jóvári, A. Piarristeguy, R. Escalier, I. Kaban, J. Bednarcik, and A. Pradel, J. Phys. Condens. Matter **25**, 195401 (2013).
[53]B. Bureau, S. Danto, H. L. Ma, C. Boussard-Plédel, X. H. Zhang, and J. Lucas, Solid State Sci. **10**, 427 (2008).
[54]D. A. Baker, M. A. Paessler, G. Lucovsky, S. C. Agarwal, and P. C. Taylor, Phys. Rev. Lett. **96**, 255501 (2006).
[55]S. Kohara *et al.*, Appl. Phys. Lett. **89**, 201910 (2006).
[56]M. Micoulaut, C. Otjacques, J.-Y. Raty, and C. Bichara, Phys. Rev. B **81**, 174206 (2010).
[57]M. Bauchy and M. Micoulaut, J. Non-Cryst. Solids **357**, 2530 (2011).
[58]M. Bauchy, M. Micoulaut, M. Celino, S. Le Roux, M. Boero, and C. Massobrio, Phys. Rev. B **84**, 054201 (2011).
[59]K. Ramesh and S. Asokan, Eur. Phys. J. B **6**, 207 (1998).
[60]A. Feltz, W. Maul, and I. Schönfeld, Z. Anorg. Allg. Chem. **396**, 103 (1973).
[61]A. Feltz, H. J. Buttner, F. J. Lippmann, and W. Maul, J. Non-Cryst. Solids **8–10**, 64 (1972).
[62]M. Anbarasu, S. Asokan, S. Prusty, and A. K. Sood, J. Appl. Phys. **105**, 084517 (2009).
[63]K. P. Lakshmi and S. Asoka, J. Non-Cryst. Solids **377**, 175 (2013).
[64]M. Anbarasu, S. Asokan, S. Prusty, and A. K. Sood, Appl. Phys. Lett. **91**, 093520 (2007).
[65]M. Anbarasu and S. Asokan, J. Phys. D **40**, 7515 (2007).
[66]M. Anbarasu, K. K. Singh, and S. Asokan, Philos. Mag. **88**, 599 (2008).

[67]C. Das, M. S. R. N. Kiran, A. Ramamurty, and S. Asoka, Solid State Commun. **152**, 2181 (2012).
[68]S. Sen, T. G. Edwards, J. Y. Cho, and Y. C. Joo, Phys. Rev. Lett. **108**, 195506 (2012).
[69]D. Selvenathan, W. Bresser, and P. Boolchand, Phys. Rev. B **61**, 15061 (2000).
[70]M. Micoulaut, Phys. Rev. B **74**, 184208 (2006).
[71]N. Manikandan and S. Asokan, J. Non-Cryst. Solids **354**, 3732 (2008).
[72]D. Derewnicka, P. Zielinski, and H. Davies, J. Mater. Sci. Lett. **1**, 87 (1982).
[73]G. G. Naumis, Phys. Rev. B **73**, 172202 (2006).
[74]M. Micoulaut, Eur. Phys. J. B **1**, 277 (1998).
[75]C. A. Angell, Science **267**, 1924 (1995).
[76]M. K. Gauer, I. Dézsi, U. Gonser, G. Langouche, and H. Ruppersberg, J. Non-Cryst. Solids **101**, 31 (1988).
[77]X. Guo, J. C. Mauro, D. C. Allan, and Y. Yue, J. Non-Cryst. Solids **358**, 1710 (2012).
[78]S. R. Aubuchon and P. S. Gill, J. Therm. Anal. **49**, 1039 (1997).
[79]S. Bhosle, K. Gunasekera, P. Boolchand, and M. Micoulaut, Int. J. Appl. Glass Sci. **3**, 205 (2012).
[80]S. Bhosle, K. Gunasekera, P. Boolchand, and M. Micoulaut, Int. J. Appl. Glass Sci. **3**, 189 (2012).
[81]Y. Tsuchiya, J. Non-Cryst. Solids **136**, 37 (1991).
[82]Y. Tsuchiya, J. Non-Cryst. Solids **312–314**, 212 (2002).
[83]R. Car and M. Parrinello, Phys. Rev. Lett. **55**, 2471 (1985).
[84]J. Akola, R. O. Jones, S. Kohara, T. Usuki, and E. Bychkov, Phys. Rev. B **81**, 094202 (2010).
[85]S. Nosé, Mol. Phys. **52**, 255 (1984); W. G. Hoover, Phys. Rev. A **31**, 1695 (1985).
[86]S. Grimme, J. Comput. Chem. **27**, 1787 (2006).
[87]M. Micoulaut, J. Chem. Phys. **138**, 061103 (2013).
[88]I. Kaban, T. Halm, W. Hoyer, P. Jòvari, and J. Neuefeind, J. Non-Cryst. Solids **326–327**, 120 (2003).
[89]F. L. R. Schoening, J. Mater. Sci. **14**, 2397 (1979).
[90]F. Kakinuma, T. Fukunaga, and K. Suzuki, J. Non-Cryst. Solids **312–314**, 380 (2002).
[91]G. E. A. Bartsch, H. Bromme, and T. Just, J. Non-Cryst. Solids **18**, 65 (1975).
[92]G. E. A. Bartsch and T. Just, Z. Metall. **63**, 360 (1972).
[93]M. Micoulaut, A. Kachmar, M. Bauchy, S. Le Roux, C. Massobrio, and M. Boero, Phys. Rev. B **88**, 054203 (2013).
[94]M. Bauchy and M. Micoulaut, J. Non-Cryst. Solids **377**, 34 (2013).
[95]P. S. Salmon, J. Non-Cryst. Solids **353**, 2959 (2007).
[96]K. Ploog, W. Stetter, A. Nowitzki, and E. Schönherr, Mater. Res. Bull. **11**, 1147 (1976).
[97]J. Kalikka, J. Akola, R. O. Jones, S. Kohara, and T. Usuki, J. Phys. Condens. Matter **24**, 015802 (2012).
[98]J. Akola and R. O. Jones, Phys. Rev. Lett. **100**, 205502 (2008).
[99]C. Bichara, M. Johnson, and J.-Y. Raty, Phys. Rev. Lett. **95**, 267801 (2005).
[100]J. Akola and R. O. Jones, Phys. Rev. B **76**, 235201 (2007).
[101]J.-Y. Raty, C. Otjacques, J. P. Gaspard, and C. Bichara, Solid State Sci. **12**, 193 (2010).
[102]S. Caravati, M. Bernasconi, T. D. Kuehne, M. Krack, and M. Parrinello, Appl. Phys. Lett. **91**, 171906 (2007).
[103]P. L. Chau and A. J. Hardwick, Mol. Phys. **93**, 511 (1998).
[104]R. Mazzarello, S. Caravati, S. Angioletti, M. Bernasconi, and M. Parrinello, Phys. Rev. Lett. **104**, 085503 (2010).
[105]M. Krbal, A. V. Kolobov, P. Fons, K. V. Mitrofanov, Y. Tameroni, J. Hegedüs, S. R. Elliott, and J. Tominaga, Appl. Phys. Lett. **102**, 111904 (2013).
[106]J. P. Itié, A. Polian, G. Calas, J. Petiau, A. Fontaine, and H. Tolentino, Phys. Rev. Lett. **63**, 398 (1989).
[107]M. Stevens and P. Boolchand, Phys. Rev. B **29**, 1 (1984).
[108]S. Raoux, W. Welnic, and D. Ielmini, Chem. Rev. **110**, 240 (2010).
[109]P. Boolchand, in *Physical Properties of Amorphous Materials*, edited by D. Adler, B. B. Schwartz, and M. C. Steele (Plenum, 1985), p. 221.
[110]S. Chakravarty, D. G. Georgiev, P. Boolchand, and M. Micoulaut, J. Phys. Condens. Matter **17**, L7 (2005).
[111]T. Qu, D. G. Georgiev, P. Boolchand, and M. Micoulaut, in *Supercooled Liquids, Glass Transition, and Bulk Metallic Glasses, MRS Symposium Proceedings No. 754*, edited by T. Egami, A. L. Greer, A. Inoue, and S. Ranganathan (Materials Research Society, Pittsburgh, 2003), p. CC8.1.1.
[112]D. G. Georgiev, P. Boolchand, and M. Micoulaut, J. Optoelectr. Adv. Mater. **4**, 823 (2002).
[113]K. Gunasekara, S. Bhosle, P. Boolchand, and M. Micoulaut, J. Chem. Phys. **139**, 164511 (2013).
[114]S. Ravindren, K. Gunasekera, Z. Tucker, A. Diebold, P. Boolchand, and M. Micoulaut, J. Chem. Phys. **140**, 134501 (2014).
[115]M. Tatsumisago, B. L. Halfpap, J. L. Green, S. M. Lindsay, and C. A. Angell, Phys. Rev. Lett. **64**, 1549 (1990).
[116]M. Bauchy and M. Micoulaut, Phys. Rev. Lett. **110**, 095501 (2013).
[117]C. Bourgel, M. Micoulaut, M. Malki, and P. Simon, Phys. Rev. B **79**, 024201 (2009).
[118]F. Wang, S. Mamedov, P. Boolchand, B. Goodman, and M. Chandrasekhar, Phys. Rev. B **71**, 174201 (2005).
[119]M. Micoulaut and G. G. Naumis, Europhys. Lett. **47**, 568 (1999).
[120]M. Micoulaut, J. Phys. Condens. Matter **22**, 285101 (2010).
[121]S. Mamedov, D. G. Georgiev, T. Qu, and P. Boolchand, J. Phys. Condens. Matter **15**, S2397 (2003).
[122]G. Yang, Y. Guegen, J. C. Sanglebœuf, T. Rouxel, C. Boussard-Plédel, J. Troles, P. Lucas, and B. Bureau, J. Non-Cryst. Solids **377**, 54 (2013).
[123]P. Boolchand, D. G. Georgiev, T. Qu, F. Wang, L. Cai, and S. Chakravarty, C. R. Chim. **5**, 713 (2002).
[124]K. Tanaka, Phys. Rev. B **39**, 1270 (1989).
[125]Y. Wang, M. Nakamura, O. Matsuda, K. Inoue, and K. Murase, J. Non-Cryst. Solids **198–200**, 753 (1996).
[126]V. G. Dittmar and H. Schäfer, Acta Cryst. B **31**, 2060 (1975).
[127]A. Pradel, V. Michel-Lledos, M. Ribes, and H. Eckert, Chem. Mater. **5**, 377 (1993).
[128]M. Celino and C. Massobrio, Phys. Rev. Lett. **90**, 125502 (2003).